Studies of Initial Atmospheric Corrosion of Magnesium Alloys AZ91 and AZ31 with Infrared Spectroscopy Techniques

Dan Persson *, Alexander Wärnheim, Nathalie Lebozec, Dominique Thierry

Posted Date: 17 September 2025

doi: 10.20944/preprints202509.1467.v1

Keywords: atmospheric corrosion; magnesium alloys; in situ infrared reflection absorption spectroscopy; infrared spectroscopical imaging; SKPFM; AFM-IR

 doi:10.20944/preprints202509.1467.v1

Article

Studies of Initial Atmospheric Corrosion of Magnesium Alloys AZ91 and AZ31 with Infrared Spectroscopy Techniques

Dan Persson [1,*], Alexander Wärnheim [1], Nathalie Lebozec [2] and Dominique Thierry [1]

[1] Research Institutes of Sweden (RISE) Isafjordsgatan 28A, 114 28 Stockholm, Sweden

[2] Institut de la Corrosion

* Correspondence: dan.persson@ri.se

Abstract

The initial formation of corrosion products in pure humid air on magnesium alloys AZ91 and AZ31 was studied using infrared reflection absorption spectroscopy (IRRAS), infrared spectroscopic imaging, and SEM-EDS. The kinetics of corrosion product formation were monitored in situ with IRRAS during exposure to humid air (95% relative humidity) under two different CO_2 concentrations: low (<1 ppm) and ambient (400 ppm). For low CO_2 concentrations, the primary corrosion product detected on both alloys was magnesium hydroxide ($Mg(OH)_2$). In contrast, under ambient CO_2 conditions (400 ppm), magnesium hydroxy carbonate was the dominant product. After 16 hours of exposure, the amount of magnesium converted into corrosion products was approximately 8-10 times higher under low CO_2 conditions compared to ambient levels. The smaller formation of corrosion products but increased magnesium carbonate formation on AZ91D is attributed to its higher aluminum content compared to AZ31. Corrosion attack and product formation were largely localized to the centre of the α-phase in AZ91D, with the β-phase likely serving as sites for cathodic reactions.

Keywords: atmospheric corrosion; magnesium alloys; in situ infrared reflection absorption spectroscopy; infrared spectroscopical imaging; SKPFM; AFM-IR

1. Introduction

Magnesium (Mg) alloys are the lightest metallic structural alloys and are of interest for a wide range of uses in the aerospace, automotives, electronic and optical equipment, telecommunication applications and for biodegradable implants. Magnesium alloys have a low density, high strength to weight ratio but also other adequate mechanical properties, including good machinability, but their range of applications can be restricted due to their poor corrosion behaviour compared to other light materials, such as aluminium alloys. Magnesium alloys are frequently used in automotive applications in interior components, such as instrumental panels, cross bar beams, seat frames, roof frames and more [1]. In the electronics industry, magnesium alloy plays an important role for shells and components of 3C devices like mobile phones, notebook computers, digital cameras, and optical equipment due to their high specific strength, high thermal and electrical conductivity, as well as excellent electromagnetic shielding properties [2]. In these applications, magnesium materials are seldom exposed to harsh and highly corrosive conditions, such as high chloride loads, but often to intermittent high humidity and moisture.

Numerous studies have been devoted to the corrosion behaviour of various magnesium alloys during the last decades. Many studies are performed in aqueous NaCl electrolyte solution and the electrochemical and corrosion properties for different alloy compositions, microstructures and surface conditions have been studied extensively, and have been summarized in several reviews [3–8]. Relatively fewer investigations have studied the corrosion behaviour of magnesium alloys under

 doi:10.20944/preprints202509.1467.v1

atmospheric conditions [9–11]. Many of these studies have been made during exposures to aggressive conditions with high chloride deposition on the surfaces or in polluted industrial atmosphere [10], although many applications of magnesium alloys involve exposure of magnesium alloys to relatively mild atmospheric conditions. Investigations of the atmospheric corrosion of magnesium alloys in high humidity but milder atmospheric conditions, without chloride and corrosive gases, have been reported in several publications [12–15]. Arrabal et al. [12] studied the atmospheric corrosion in humid conditions for Mg/Al alloys and found that both aluminium content and alloy microstructure influenced corrosion. M. Shahabi-Navid et al. [13] studied the initial atmospheric corrosion of Mg/Al alloys in humid air, with low and ambient CO2 content in the air and it was concluded that the surface film formed was thinner after exposure in the presence of CO2 compared to when CO2 was absent. It was also observed that alloy AZ91 exhibited significantly less localised corrosion in humid air than alloy AM50 and pure magnesium. In another study, it was shown that the mass gain of pure magnesium exposed in humid air was higher for low CO2 content [15]. Several studies have shown that the atmospheric corrosion rate decreases for higher aluminium content in the alloy. The effect of aluminium has been attributed to several factors, the influence Al of the surface film, which could slow down the corrosion in the initial stages. Secondly, microgalvanic coupling of b-phase which can initially cause accelerated attack on the a-Mg but as the corrosion attack proceeds the fraction of the aluminium rich b-phase increase at the surface exposed to the corrosive medium. This leads to an overall decrease of the corrosion rate with the b-phase acting as physical barrier against corrosion attack and hinder corrosion propagation in the matrix [16,17]. For studies of the initial stages of the atmospheric corrosion under milder conditions, the latter is probably less relevant and the effect of aluminium on the stability of the initial surface oxide / surface film related to variations in the aluminium content of different alloys should be more important. It has been suggested that the effects of Al content are associated with an Al-enriched layer which has been detected in the thin surface film on Mg/Al alloys [13,18–20]. It was found that Al can diffuse and be incorporated into a Mg-oxide/hydroxide during atmospheric corrosion [20]. Studies of atmospheric corrosion of metals under atmospheric conditions are difficult to perform with conventional electrochemical techniques due the thin water layer on the surface formed under atmospheric conditions, in particular, when soluble salts are absent on the surface. Infrared spectroscopy is a powerful method for identifying corrosion and reaction products formed during atmospheric corrosion of metals under in situ conditions and can also provide information about the kinetics of corrosion product formation upon exposure in humid air [21,22]. FTIR-microscopy and imaging can be used for chemical imaging of corrosion products related to the microstructure of a material [23] which can provide a deeper understanding of corrosion mechanisms. The recent development of nanoscale infrared microscopy has overcome the diffraction limited restriction in lateral resolution for conventional optical IR-microscopy and can provide information about corrosion product formation with submicron and nanoscale resolution [24].In the present work, the initial atmospheric corrosion on AZ91 and AZ31 during 19 h exposure in humid air was studied using in situ infrared reflection absorption spectroscopy (IRRAS) to provide information about corrosion products composition and their kinetics of formation. Complementary infrared chemical imaging of the local products formation was obtained by FTIR-ATR FPA chemical imaging and AFM-IR. Additional SEM-EDS measurements were employed to determine the localisation of the corrosion attacks and the morphology of corrosion products. The main objective was to provide more comprehensive view of the initial corrosion products formation in humid air.

2. Materials and Methods

2. Experimental

2.1. Materials

The materials studied were two commercial alloys with different aluminium content e.g., AZ 31 and AZ91 with nominal compositions given in Table 1. The microstructures of the materials studied here are shown in Figures 1 and 2. The AZ91 D has a dendritic solidification microstructure with very

 doi:10.20944/preprints202509.1467.v1

clear dendrites and secondary phases in the inter-dendritic spacings. Al and Zn are strongly segregated and the main the secondary ◎◎phase consists of Al12Mg17. AAZ31 has a somewhat mixed grain structure with main AlMn intermetallic particles and some particles contains Zn (and Al), mainly at grain boundaries. The samples used for in situ IRRAS-measurements were sequentially with the last step using # 4000 grinding paper, while samples used for FTIR-FPA imaging and AFM-IR were diamond polished to 1 ◎m.

Table 1. Nominal composition in wt% of tested materials.

material	Al	Zn	Mn	Si	Cu	Fe	Ni
AZ 31	3.1	0.73	0.25	0.02	<0.001	0.006	<0.001
AZ 91	8.8	0.68	0.3	0.001	0.0	0.004	<0.004

2.2. Exposure Conditions

The exposures of the samples were performed with pure humid air containing a low content of CO2, (<≈ 1 ppm) as produced by a FTIR purge gas generator (adsorption dryer). Humid air with 95 % ±2% RH was produced by mixing dry air and humidified air at 98-99 % RH in an apparatus as described previously [21].

2.3. In Situ Infrared Reflection Absorption Spectroscopy

In situ Infrared reflection absorption spectroscopy (IRRAS) during exposure to humid air was performed using an experimental set-up which allows measurements at grazing angle (78º) on the metal surface using p-polarised light [21]. The in situ measurements were performed in a stainless steel cell with ZnSe windows with infrared spectrum recorded after 5 minutes and then each 30 minutes after the introduction of the humid air into the cell. In situ spectra of the corrosion products formed on the surface were obtained by subtracting the spectra after different time with the first spectrum recorded after 5 minutes. This removes the water bands from the water molecules in the gas phase in the exposure cell, form the spectra. The air flow through the cell was 1 liter / minute. Optical simulations of IRRAS spectra were conducted with the transfer matrix method using Matlab. Transmission spectra used for the calculations were made by mixing the compounds with KBr and recording transmission spectra of a pressed tablet [21,22].

2.4. FTIR-ATR FPA Imaging

FTIR imaging was performed using a Bruker Vertex 70 spectrometer equipped with a Hyperion 3000 microscope (Bruker Optics, Ettlingen, Germany) with a 64 × 64 focal plane array (FPA) detector. FTIR-FPA imaging was performed in the attenuated total reflectance (ATR) mode with 20× ATR objective equipped with a 100 µm diameter Ge internal reflection element. The field view is ≈ 33 × 33 µm² using the Ge-ATR objective corresponding to a pixel resolution of ≈ 0.5 µm. Infrared spectra were acquired in the region 880 to 3860 cm^{-1} by adding 500 scans at 8 cm−1 resolution.

2.5. AFM-IR

Atomic Force Microscopy-InfraRed (AFM-IR) measurements were performed in contact mode using resonance enhanced AFM-IR with a Bruker NanoIR 3. The light source was a MIRCAT POINT spectra QCL Laser (4 chip) with a spectral range of 800-1800 cm-1. IR-images were recorded by measuring at a fixed wavelength using phase locked loop. A gold coated contact NIR-probe (Bruker) with a resonance frequency of 13±4 kHz was used for AFM-IR measurements. AFM-IR spectra were measured with 2 cm-1 spectral resolution. Laser power during spectral acquisition and IR-imaging, was ≈15 % of the maximum laser power of approximately 800 mW. Step discontinuities which occur

 doi:10.20944/preprints202509.1467.v1

when the QCL laser shift between the 4 chips which results in sharp steps in the broad band spectra were corrected by post processing the spectra using the Analysis Studio software. During AFM-IR measurements, dry nitrogen was flowing through the AFM-IR instrument to minimize contributions from water vapor and CO_2 in the spectra.

2.6. Scanning Kelvin Probe Force Microscopy (SKPFM)

The variation in Volta potential along a unexposed polished (0.25 mm diamond) AZ91 surface was measured using a Bruker NanoIR3 system with an SKPFM attachment. The probes had resonant frequencies of 47 – 76 kHz, spring constants in the range of 1.2 – 6.4 N/m and a 25 ± 5 nm thick conductive Pt/Ir coating. Areas of interest, containing both beta and alpha phase, were identified using the attached optical microscope. The Volta potential maps are presented as potential with respect to the sample and the values were offset to be centred around 0V.

2.7. SEM-EDS

Field Emission Gun – Scanning Electronic Microscope (FEG-SEM) equipment used was a LEO 1530 with Gemini column, upgraded to a Zeiss Supra 55., with a 50mm2 X-Max Silicon Drift Detector (SDD) from Oxford Instruments EDS detector.

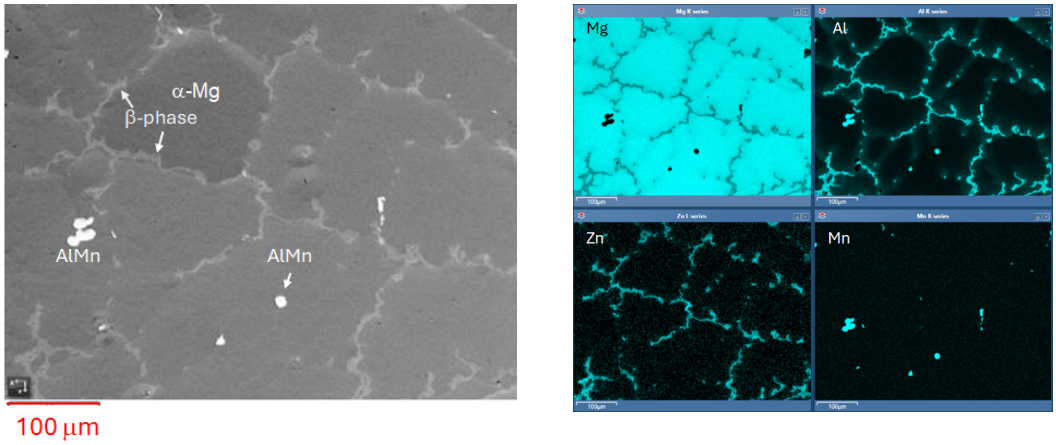

(**a**) (**b**)

Figure 1. SEM image a) and SEM-EDS maps b) of AZ91 prior to exposure.

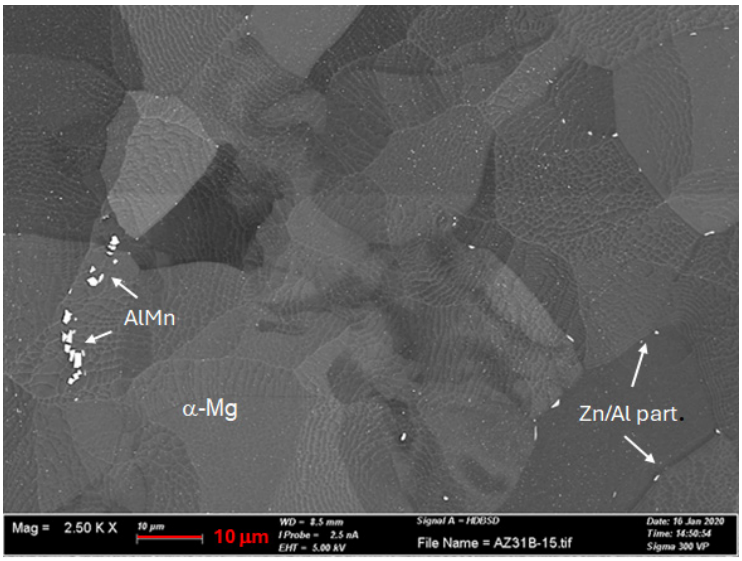

 doi:10.20944/preprints202509.1467.v1

Figure 2. SEM image of AZ31 prior to exposure.

3. Results

3.1. In Situ Infrared Reflection Absorption Spectroscopy

IRRAS absorption spectra of the AZ91 during exposure to humid air with low and ambient CO2 content are shown in Figure 3. The spectra obtained in low CO_2 atmosphere show a sharp peak at 3704 cm^{-1} which is due to hydroxyl stretching of $Mg(OH)_2$ [25,26], a broad asymmetric band with a maximum at 600 cm^{-1} mainly attributed to Mg-O vibrations in $Mg(OH)_2$ .A weaker band at ≈1450 cm^{-1} is due to asymmetric stretching vibrations of carbonate ions (CO32-) in the corrosion products. A band at 1600 cm-1 can be explained by the presence of water molecules in the corrosion products or adsorbed on the corrosion products that covered the surface. Contributions from carboxylate ions originating from volatile organic acids cannot be excluded [27,28]. On AZ91 sample exposed in humid air with ambient (≈400 ppm) CO_2 concentration, $Mg(OH)_2$ was not detected. Instead, a stronger band from carbonate around 1470 cm^{-1} was present in the spectra and, in the hydroxyl stretching region bands at 3650 cm^{-1} and 3380 cm^{-1}. These bands could originate from a poorly crystalline magnesium hydroxy carbonate, such as hydromagnesite, $Mg_5(CO_3)_4(OH)_2{\cdot}5H_2O$ [25,26]. The experimental spectra obtained for AZ91 D can be compared with calculated IRRAS spectra of $Mg(OH)_2$ and in Figure 4.

It cannot be ruled out that there are some contributions from MgO for the asymmetric band with the maximum at 602 cm^{-1}. the LO-mode of MgO, which has been reported to be located at 718 cm^{-1} [24] and 737 cm^{-1} [29]. This vibrational mode should be visible in IRRAS spectra recorded at grazing angle [30]. Calculated IRRAS of MgO on a Mg surface indeed have a strong band at 738 cm^{-1}. However, the similarity between calculated IRRAS spectra of $Mg(OH)_2$ in Figure 4 and the spectra obtained during exposures with low CO_2, with an asymmetric band with a maximum at 612 cm^{-1} and 602 cm^{-1}, respectively, indicates that the spectra for the Mg-alloys exposed at low CO_2 level is mainly explained by $Mg(OH)_2$.

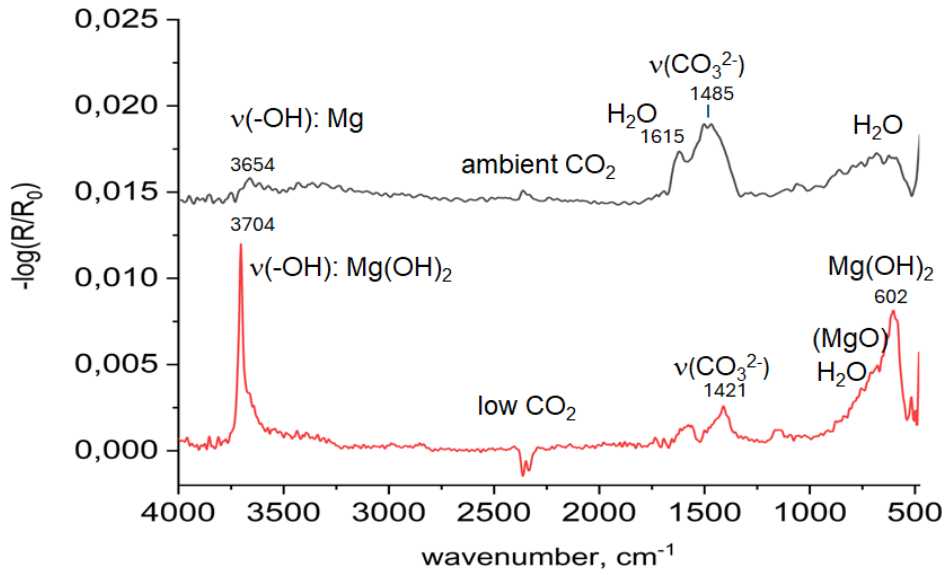

Figure 3. In situ Infrared Reflection Absorption Subtraction Spectra for AZ91 after 5 h of exposure in humid air (94 % RH) with low CO_2 (<1 ppm) and ambient CO_2 (≈ 400ppm).

For AZ31 alloy, the spectra are similar for low CO_2 content in the humid air with formation of $Mg(OH)_2$ and weak bands from carbonate, see Figure 5. The spectra obtained at ambient CO_2 level

 doi:10.20944/preprints202509.1467.v1

have also a weak peak at 3704 cm^{-1} due to $Mg(OH)_2$ and hydroxyl and carbonate bands associated with formation of magnesium hydroxy carbonate.

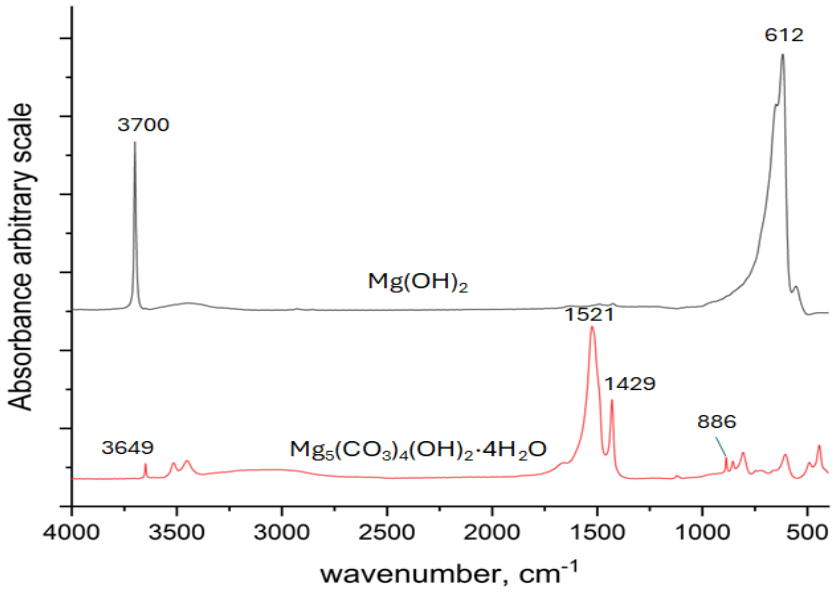

Figure 4. Calculated IRRAS spectra of $Mg(OH)_2$ and $Mg_5(CO_3)_4(OH)_2{\cdot}4H_2O$ on a magnesium substrate.

Formation of magnesium hydroxy carbonate, hydromagnesite ($Mg_5(CO_3)4(OH)_2{\cdot}4H_2O$ was detected after 28 days exposure to humid air by Arrabal et al. [12]. Zinc hydroxy carbonates such as hydromagnesite [13] and dypingite ($Mg_5(CO_3)4(OH)_2{\cdot}4H_2O$ {13,15] have been reported in previous exposures after exposure on humid air.

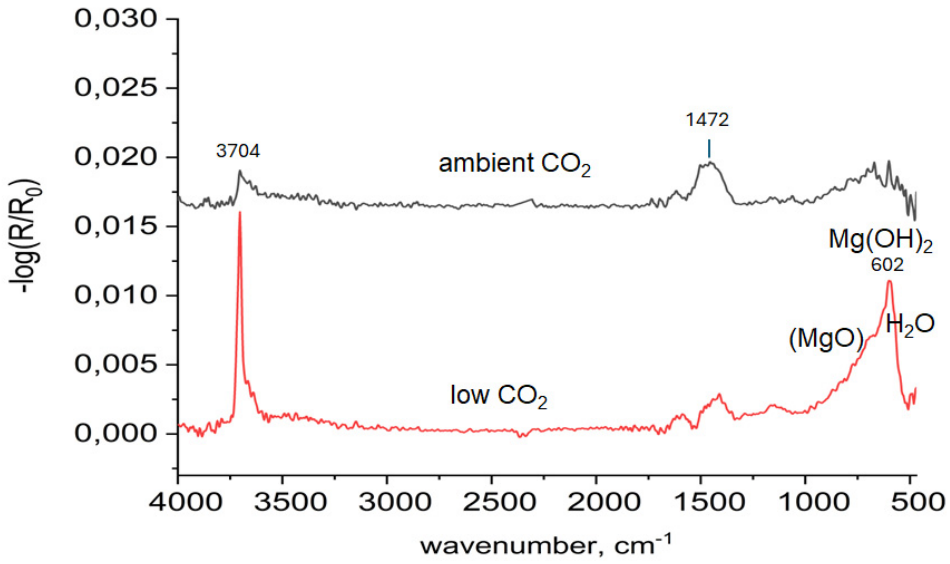

Figure 5. In situ Infrared Reflection Absorption Subtraction Spectra for AZ31 after 5 h exposure in humid air (94 % RH) with low CO_2 (<1 ppm) and ambient CO_2 (≈ 400ppm).

A detailed comparison of the spectra on the hydroxyl stretching region are shown in Figure 6, together with reference spectra of brucite ($Mg(OH)_2$) and hydromagnesite, ($Mg_5(CO_3)_4(OH)_2{\cdot}4H_2O$). The sharp hydroxyl band associated with $Mg(OH)_2$ is clearly present for AZ91 and AZ31 after

 doi:10.20944/preprints202509.1467.v1

exposure in humid air with low CO_2 content, but also for AZ31 exposed at ambient CO_2. However, for AZ91 exposed at ambient CO_2, a peak around 3650 cm^{-1}which has a similar position as that of hydromagnesite ($Mg_5(CO_3)_4(OH)_2{\cdot}4H_2O$ may be observed. However, the other characteristic bands at 3520 and 3450 cm^{-1} for $Mg_5(CO_3)_4(OH)_2{\cdot}4H_2O$ are not clearly discerned in the IRRAS-spectra of the surface which could be due to the formation of more disordered of magnesium hydroxy carbonate at this stage of exposure.

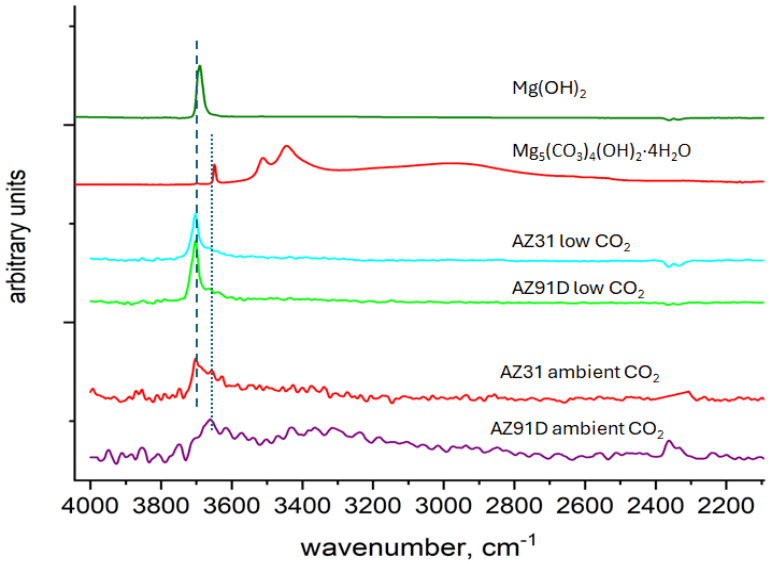

Figure 6. Comparison of spectra (hydroxyl stretch region 4000-2200 cm^{-1}) for AZ31 and AZ91 after exposure with reference spectra of $Mg(OH)_2$ and $Mg_5(CO_3)_4(OH)_2{\cdot}4H_2O$.

By plotting the intensities of different IR-bands in the spectra, information about the kinetics of corrosion products formation may be obtained. Figure 7 show the intensities of the hydroxyl stretching band for $Mg(OH_2$ at 3704 cm^{-1} and the carbonate band on the region 1400-1 500 cm^{-1} vs exposure time for the two different alloys and exposure conditions. The kinetics of corrosion show a rapid formation of corrosion product during the first 8 hours of exposure with a decreasing rate of formation after 8-1 0 h exposure.

The intensities of $Mg(OH)_2$ are clearly higher for AZ31 which has a lower aluminium content, while the carbonate bands are higher for AZ91 compared to AZ31 in humid air with ambient CO_2 content.

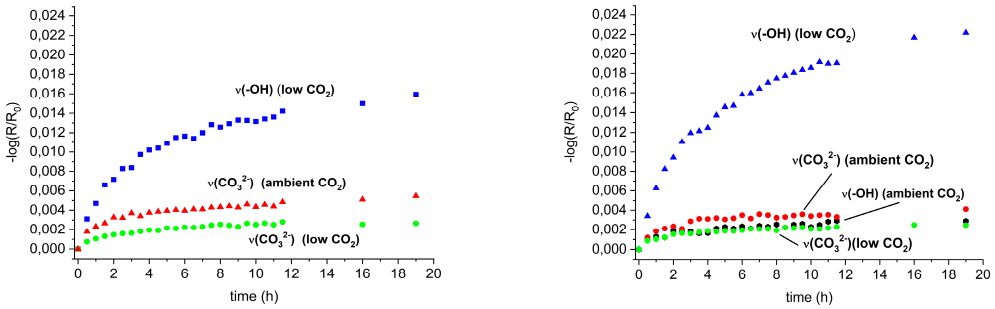

(**a**) (**b**)

Figure 7. Intensities (-log(R/R0) of hydroxyl at 3704 cm^{-1} ($Mg(OH)_2$) and Mg-carbonate (1400-1 500 cm^{-1}) vs exposure time for AZ91 a) and AZ31 b).

 doi:10.20944/preprints202509.1467.v1

The IR-intensities vs time for the corrosion products formed was used to roughly estimate the amount of metallic magnesium converted into corrosion products, assuming that they mainly consist of $Mg(OH)_2$ and $Mg_5(CO_3)_4(OH)_2{\cdot}4H_2O$. Estimation of the average thickness of the coating product layers was made using an approximate version of Francis and Ellisons equation [31] for the intensity of a band in reflection-absorption spectra for a certain thickness of the surface film on a metal surface of a good reflector:

$$-\log\left(\frac{R}{R_0}\right) \approx \frac{4n_1 \sin\theta \tan\theta}{\ln 10 \cdot n_2^3}\,\alpha d \qquad (1)$$

With d:average thickness of surface film, n_1: the refractive index of the surface film, n2: refractive index of the surface film, α: the absorption coefficient of the actual IR-band of the surface film. The absorption coefficients for the hydroxyl stretching peak of $Mg(OH)_2$ and the carbonate asymmetric stretching band for carbonate in $Mg_5(CO_3)_4(OH)_2{\cdot}4H_2O$ were estimated from transmission spectra of these compounds. The amount of Mg formed in the corrosion products is considerably higher during exposure in humid air with low CO_2 content, as seen in Figure 7. The corrosion products formation is also higher on AZ31 compared to AZ91, which is in accordance with the results by Arrabal et al. who showed that alloys with higher aluminium content (AZ80 and AZ91D) presented lower mass gain values compared to AZ31 and pure Mg. Similar results were obtained by Feliu Jr et al. [14] with 2 times lower mass gain for AZ91 compared to AZ31 after exposure in air with 98 % RH. At the same time, higher Al-content resulted in increased carbonate formation and less MgO /$Mg(OH)_2$. Studies of the effect of low and ambient levels of CO2 for pure magnesium showed that the mass gain was approximately 4 times higher after 4 weeks exposure in humid air with low CO2 content compared air with 330 ppm CO2 which is in line with the present results [15]. Thinner surface films were formed on Mg / Al alloys in the presence of higher CO2 content in the humid air for short term exposures [13]. Thus, the results obtained in this work are consistent with previous studies of magnesium and magnesium alloys in humid conditions.

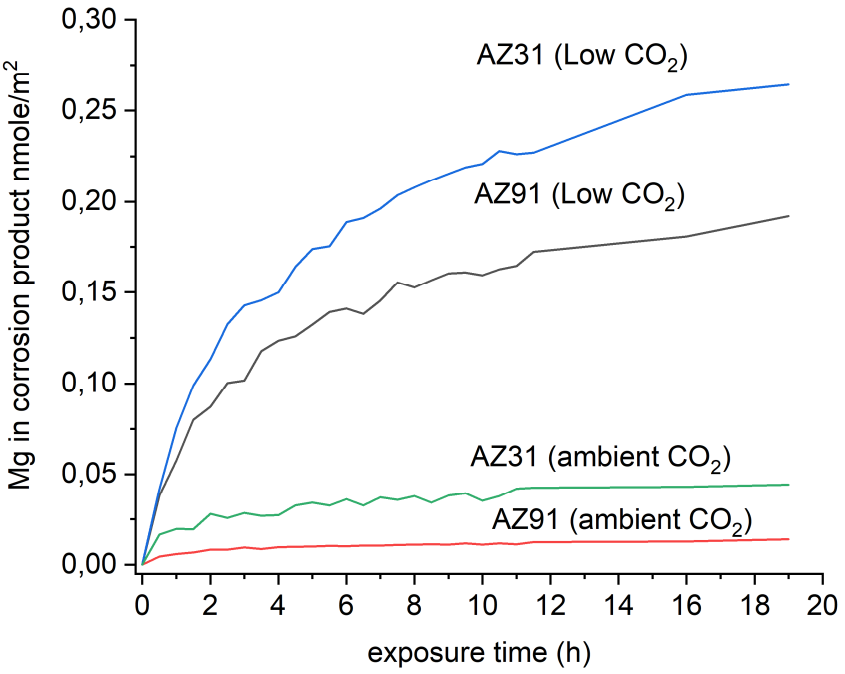

Figure 8. Magnesium formed in corrosion products (assumed to consist of $Mg(OH)_2$ + $Mg_5(CO_3)_4(OH)_2{\cdot}4H_2O$) during exposure to humid air in low and ambient CO_2 of AZ31 and AZ91 estimated from in situ IRRAS measurements.

 doi:10.20944/preprints202509.1467.v1

3.2. SEM-EDS

After exposure, the surfaces were examined by SEM. Figure 9 show SEM-images of AZ91 exposed in humid air with ambient and low CO2 content in the air showing corrosion attack in the a-phase. The severity of the attacks with numerous initiation points seems to be located largely to the interior of α-grains while a zone in the α-phase close to the β-phase is much less affected by corrosion attack. For the AZ31 alloy, the corrosion seems also to be initiated in α-Mg phase but not directly in the vicinity of the bright intermetallic particles. Preferred attacks towards middle of the α-phase have been observed for AZ91 after humid exposures [12] and AM50 after short exposure in NaCl electrolyte [19]. The preferential attacks in the centre of the grains were attributed to the Al content in the α-phase which decreased from the vicinity of the b-phase towards the centre of the grains. Detailed studies of the AM50 alloy by Schwarz et al**.** [20] using atom probe tomography revealed that a thin Al-rich layer was present beneath an amorphous MgO and $Mg(OH)_2$, at the alloy/oxide interfaces under the atmospheric corrosion of a magnesium alloy. However, they could not find evidence for the formation of an aluminium oxide layer.

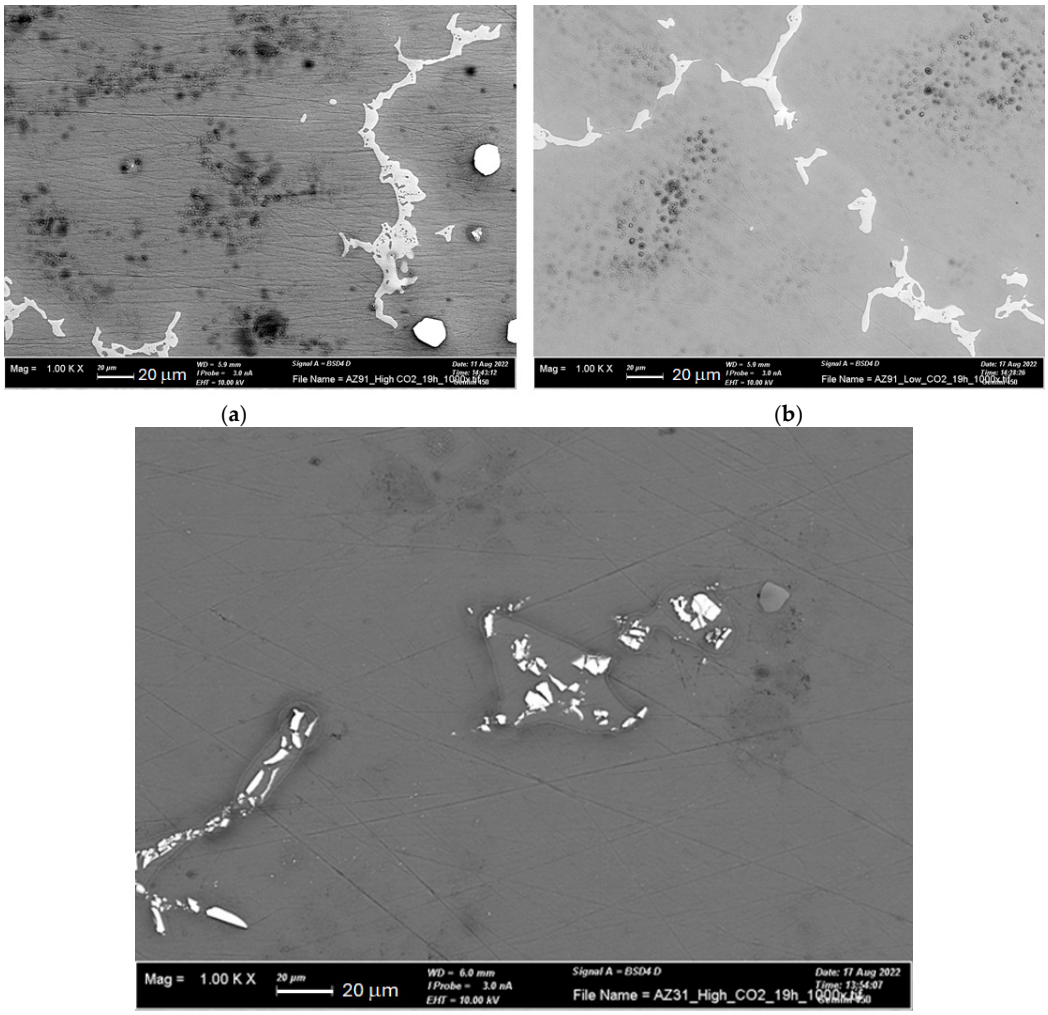

Figure 9. SEM images of AZ 91 exposed 19h in humid air (95% RH) with ambient CO_2 content a) and low CO_2 content b), and AZ 31 exposed 19 h in humid air (95% RH) c).

SEM-EDS analysis of AZ 91 exposed 19h in humid air (95% RH) with ambient CO_2 content in Figure 10 indicate a lower aluminium content in the area with preferential corrosion attacks compared to areas closer to the β-phase, which has been observed in a previous study of the same

 doi:10.20944/preprints202509.1467.v1

alloy [12]. In the corroded areas, both the carbon and oxygen content are enhanced which is consistent with the formation of magnesium hydroxide carbonate as detected by IRRAS.

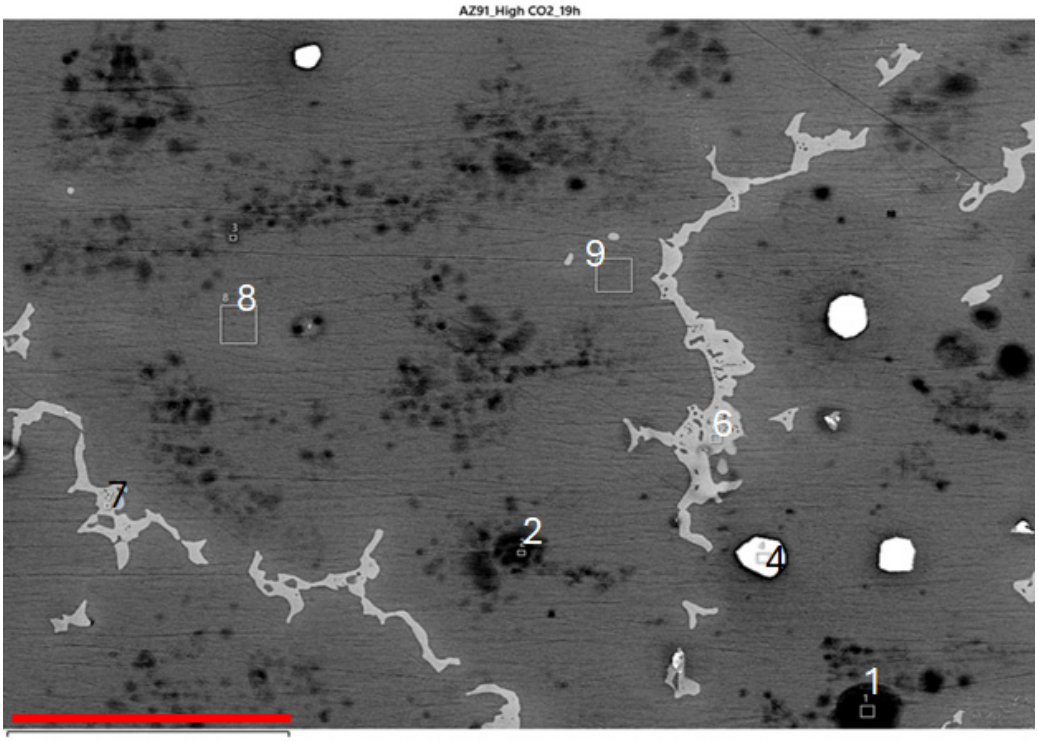

Area	Mg at%	Al at%	O at %	C at %	Mn at%
1	71.26	2.66	19.35	6.74	
2	79.67	2.04	14.05	4.25	
4	0.66	52.08	2.7	0.83	42.5
6	59.71	35.56	1.73	1.15	
7	61.03	34.96	1.37	0.92	
8	91.81	5.87	1.01	1.31	
9	91.35	6.49	1.22	0.94	

Figure 10. SEM image and EDS elemental analysis of AZ91 exposed 19h in humid air (95% RH) with ambient CO_2.

For AZ31, the corrosion attacks were also mainly localised a distance from the intermetallic particles and numerous initiation points observed for AZ91 seems to be absent. A more uniform corrosion of AZ31 compared to AZ91 was observed by Arrabal et al. for longer exposures in humid air [12].

When the surfaces at corrosion attacks are examined in detail, a striking difference may be observed., see Figure 11. The corrosion products formed with ambient CO_2 content, which mainly consist of magnesium hydroxy carbonate, seem to form compact looking layer on the surface at the corrosion initiation sites. On the other hand, the $Mg(OH)_2$ corrosion products formed with low CO_2 content have a different morphology with more porous sponge-like looking structure, growing outwards from the surface. Similar corrosion product morphology was also observed for corrosion of pure Mg in humid exposures with low CO_2 content by Lindstrom et al. [15]. The morphology of

 doi:10.20944/preprints202509.1467.v1

the $Mg(OH)_2$ indicates that this product is less protective and porous compared to the magnesium hydroxy carbonate, which can lead to a higher corrosion rate in low CO2 conditions.

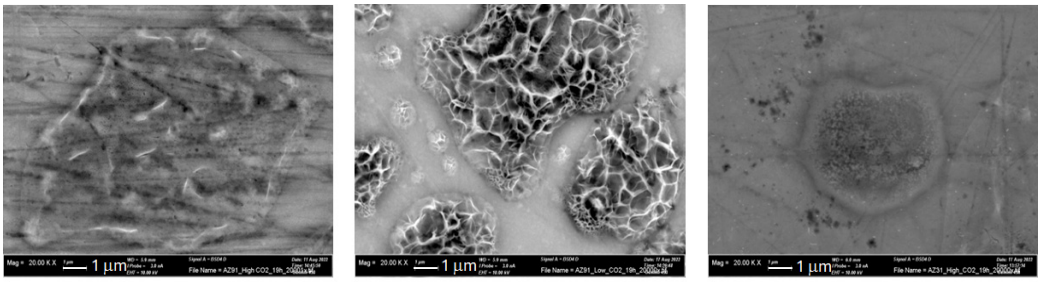

(**a**) (**b**) (**c**)

Figure 11. SEM images with high magnification in areas where corrosion products are located on AZ91 exposed 19 h in humid air with a) ambient CO_2, b) low CO_2 and c) AZ31 exposed 19 h in humid air with ambient CO_2.

3.3. Infrared Spectroscopy Chemical Imaging

The exposed sample surfaces were also studied with FTIR-ATR FPA chemical imaging, which can provide information about the distribution of the corrosion products on the alloy surface. Chemical images of the carbonate band at 1470 cm^{-1} for AZ91 after 5 and 19 h exposure show that the carbonate containing corrosion product is formed on the α-Mg and nothing or very small amounts on the β-phase, as seen in Figure 12.

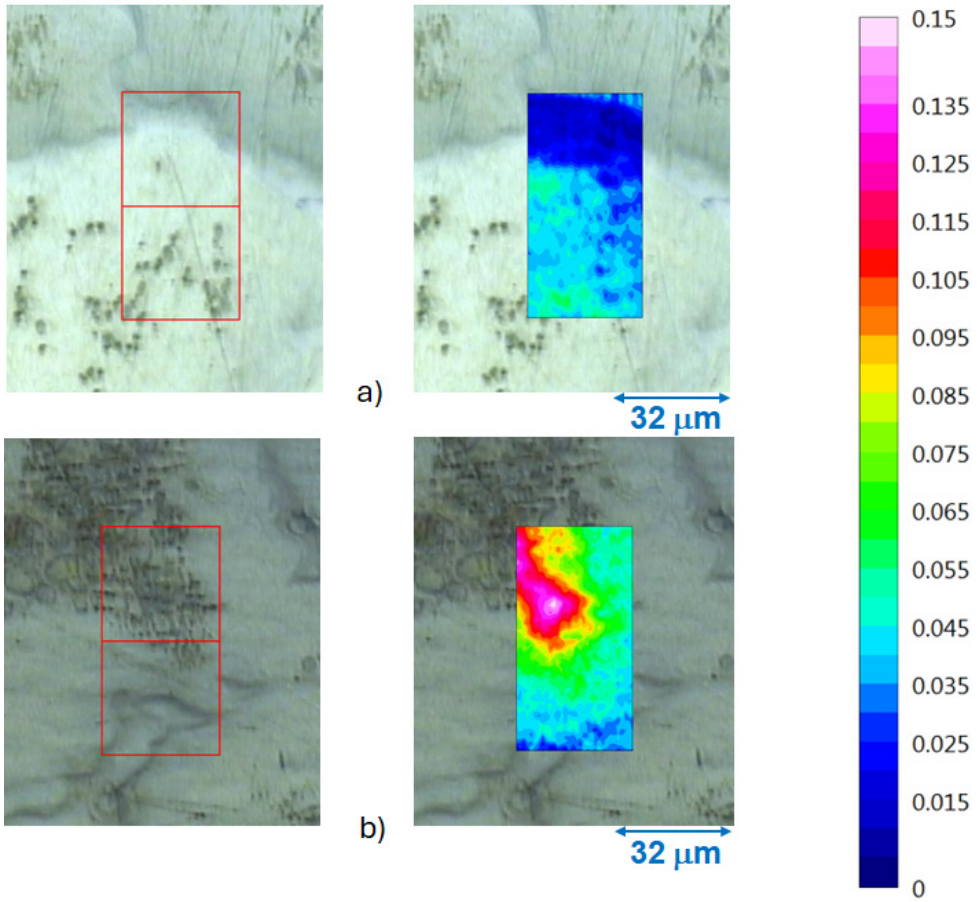

 doi:10.20944/preprints202509.1467.v1

Figure 12. FTIR-ATR FPA chemical imaging of AZ91 after a) 5 h and b) 19 h of exposure in humid air (95%) with ambient CO_2 content. Optical images of the surface (to the left) and false colour images of the carbonate band at 1470 cm^{-1} overlaid the optical images.

The chemical and optical images also indicated how the amount of corrosion products increases with exposure time. Similar results are also observed for low CO2 conditions where the distribution of Mg(OH)2 in the surface is shown in Figure 13.

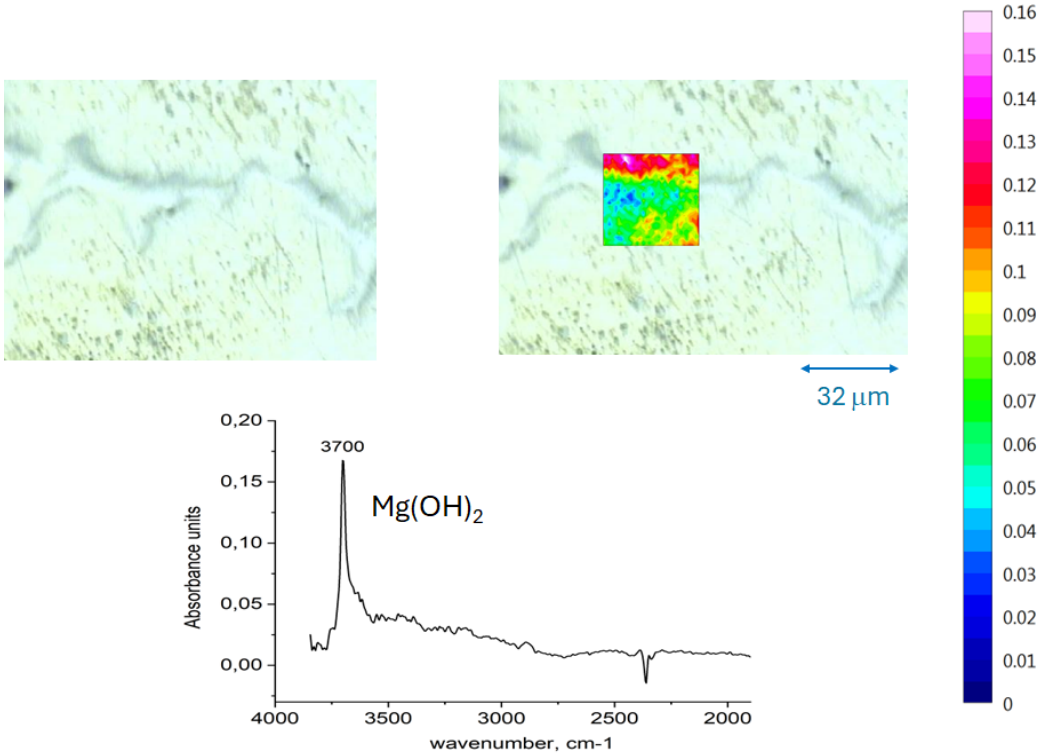

Figure 13. FTIR-ATR FPA chemical imaging of AZ91 exposed 19 h exposure in humid air (95%) with low CO_2 content. Optical images of the surface (to the left) and false colour images of the intensity of the hydroxyl stretching band of $Mg(OH)_2$ overlaid the optical images.

The surface of AZ91 exposed to humid air at ambient CO_2 content was also investigated with AFM-IR in an area where the corrosion product /corrosion attack was observed. The topographical image and the IR-image of the carbonate band at 1420 cm^{-1} is shown in Figure 14. A corrosion product cluster is seen, together with numerous submicron / nanosized corrosion initiation sites. These are located mainly at the scratches on the surfaces created by the polishing process. The AFM-IR results show that there are numerous corrosion initiation sites within the active area, and that the corrosion is initiated at many sites in the attacked area, and not in a few single pit-like attacks. Initiations could be related to sites at the scratches with enhanced dissolution at defect sites and dislocation loops produced during the grinding process [32]. The presence of the scratches might also promote water clustering [33] and formation of microdroplets of water, which initiate corrosion attack.

 doi:10.20944/preprints202509.1467.v1

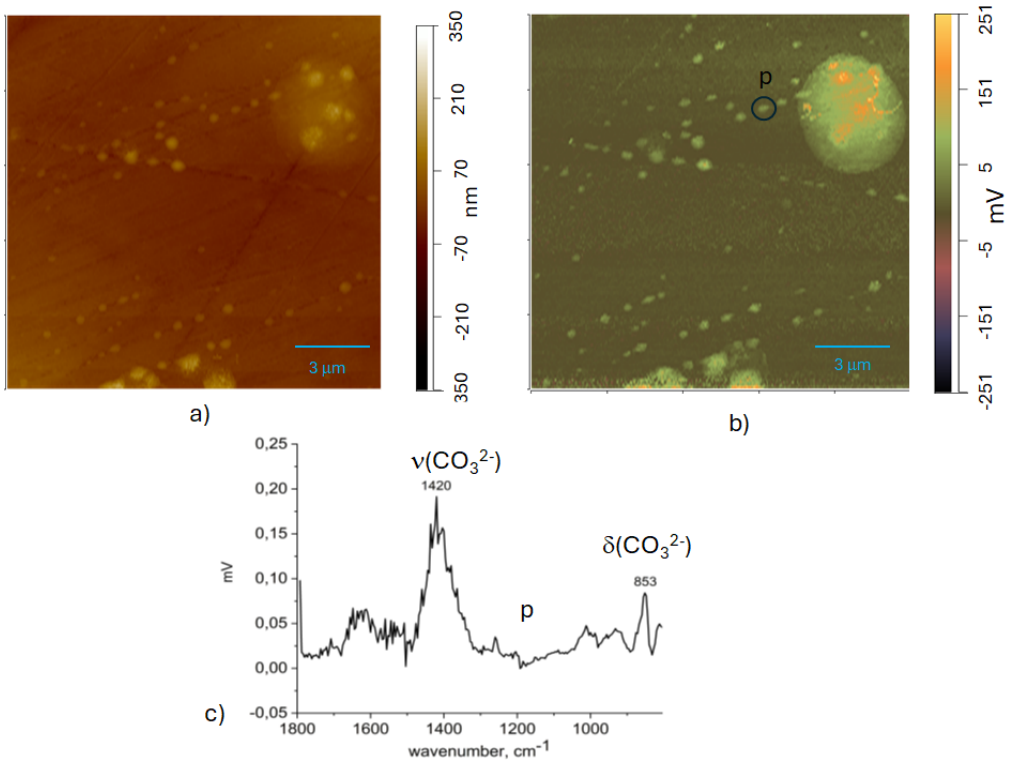

Figure 14. AFM-IR measurements on the area with corrosion attack for AZ91 after 5 h exposure in humid air with ambient CO_2 content.

3.4. Scanning Kelvin Probe Force Microscopy Measurements

SKPFM was employed to study the Volta potential variations in AZ91, focusing on different microstructural features on the surface of unexposed samples. These measurements can provide insights into the likelihood of forming micro-galvanic couples between more noble constituents and components in the microstructure with lower Volta potential. Figure 14 presents Volta potential maps and line profiles showing the potential differences (ΔV) between α-Mg and the β-phase, as well as for AlMn intermetallic particles. The Volta potential difference between the β-phase and the central regions of the α-Mg grains were in the range from 100 to 150 mV, whereas the difference between the β-phase and the α-Mg grains in its vicinity is much smaller.

The Volta potential line profiles indicate a potential gradient within the α-Mg phase near the more noble phases. This gradient is likely linked to the observation that corrosion tends to initiate in the central regions of the α-Mg grains. For AlMn particles, the ΔV between them and the α-Mg phase is higher, consistent with previous findings [12,35]. The Volta potential differences between the various phases are slightly lower compared to earlier studies [35,36]. Arrabal et al. [12] reported only minor differences between α-Mg and the β-phase, but their SKPFM measurements were limited to 5–7 µm into the α-Mg from the interface between the two phases. This is consistent with the results obtained here with low Volta potential differences close to the β-phase. However, they did observe a gradient in Al content within the α-Mg near the β-phase, which is also supported by the SEM-EDS measurements in this study.

This gradient in Al content could explain the small Volta potential differences observed near the β-phase. In contrast, the central regions of the α-Mg grains exhibit a higher ΔV, sufficient to form micro-galvanic couples. It should be noted that there is no corrosion attack localised in the proximity of the AlMn particles despite the large potential difference between AlMn and the α-Mg in close to these particles.

 doi:10.20944/preprints202509.1467.v1

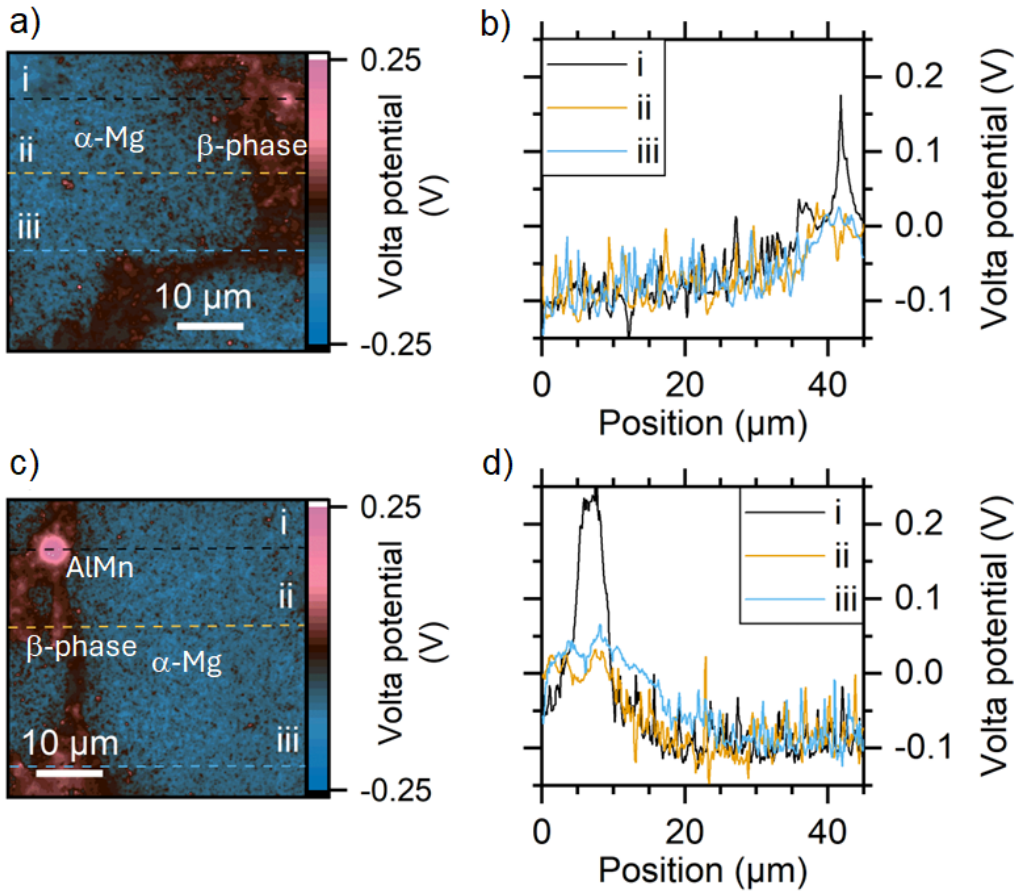

Figure 15. Volta potential maps of unexposed AZ91 surfaces a), c) and 3 Volta potential line profiles b) and d) on each area.

4. Discussion

The results of the surface analysis of corroded magnesium alloys using IRRAS, SEM-EDS and IR-spectroscopy imaging show that the corrosion is initiated on the α-Mg phase, and in the central parts of the grains for AZ91:

$$Mg \rightarrow Mg^{2+}(aq) + 2e^- \quad (2)$$

Main sites for the cathodic reaction are for AZ91 probably the β–phase on which oxygen reduction can take place according to:

$$O_2+4e^-+2H_2O \rightarrow 4OH^-(aq) \quad (3)$$

Water reduction may also contribute to the cathodic process according to:

$$H_2O +2e^- \rightarrow H_2(g) + 2OH^-(aq) \quad (4)$$

Formation of hydroxyl ions will cause alkalinisation of the surface electrolyte which affects the type of corrosion products that can be formed and may also dissolve aluminium containing surface oxides on the β-phase [34], which can facilitate the cathodic reactions on the b-phase and contribute to the higher corrosion in low CO_2 content.

In exposures in humid air with ambient CO_2 content, absorption of CO_2 in the thin adsorbed water layer will occur. The following reactions describe the equilibria for CO_2 in water:

$$H_2CO_3(aq)+OH^- \rightarrow HCO_3^-(aq) +H_2O \quad (5)$$

$$HCO_3^-(aq) +OH^- \rightarrow CO_3^{2-}(aq)+H_2O \quad (6)$$

Formation of $Mg(OH)_2$ and magnesium hydroxy carbonate can occur by ion-pairing and precipitation on the surface electrolyte layer by the following dominating reaction in low CO2 content humid air:

$$Mg^{2+}(aq) + 2OH^-(aq) \rightarrow Mg(OH)_2 \quad (7)$$

 doi:10.20944/preprints202509.1467.v1

Both the cathodic reaction routes give rise to alkalinisation of the surface electrolyte which promote the formation of $Mg(OH)_2$ at low CO_2 content in the air. In humid air with ambient CO_2 content, the formation of zinc hydroxy carbonate prevails as highlighted by the following equation:

$$5Mg^{2+}(aq) + 6OH^{-}(aq) + 4HCO_3^{2-}(aq) \rightarrow Mg_5(CO_3)_4(OH)_2{\cdot}4H_2O \quad (8)$$

As seen from the IRRAS results, a small amount of $Mg(OH)_2$ also formed on AZ31 during exposure in humid air with low CO_2 content, while $Mg(OH)_2$ was not detected on AZ91. Furthermore, larger amount of magnesium hydroxy carbonate was found on AZ91 compared to AZ31 at ambient CO_2 concentrations. This indicates that the Al-content in the alloys affects the composition of the corrosion products formed. This is in line with the study by Feliu et al. which found that increasing Al-content in the alloys leads to more magnesium carbonate formation and less MgO and $Mg(OH)_2$ [14]. The suppression of $Mg(OH)_2$ formation could be related to an effect of Al^{3+} ions dissolving from the surface film into the surface electrolyte layer. This could affect the pH and promote the formation magnesium carbonates. It is clear from the IRRAS measurements that the rate of formation of $Mg(OH)_2$ is higher for AZ31 compared to AZ91. This could probably be linked to a lower protective ability of the surface oxide/ surface film on AZ31 due to the lower Al-content in the surface film on this alloy.

The effect of the CO_2 content is large and can be related to the protective properties of the corrosion products formed. As seen in Figure 9, the corrosion products formed on AZ91 at low CO_2 content seems to have a porous sponge-like looking structure, which probably is less protective and promote further corrosion. Furthermore, the solubility of $Mg(OH)_2$ is higher (log K_s= -17.1) [37] compared to, for instance, hydromagnesite $Mg_5(CO_3)_4(OH)_2{\cdot}4H_2O$ (log K_s= -37.08) [38] which can lead to a higher ionic content in the thin water layer, higher ionic conductivity and a lower water activity. The latter will promote further water uptake in the surface electrolyte and lead to the formation of thicker electrolyte layer which stimulates the corrosion process.

Although water reduction often is considered to be the dominating cathodic reaction in aqueous conditions, it has been found that oxygen reduction is an important contributor to the cathodic process under atmospheric conditions [39,40] but also in electrolyte solution [41,42]. For AZ91, the β-phase is probably the cathodic area, and as indicated by the results of SEM-EDS, IR-chemical imaging, the formation of corrosion products is low on the β-phase and the cathodic processes can be sustained during prolonged exposures. The Volta potential difference between the β-phase and the centre of the α-Mg phase was 100-150 mV which could be enough for the formation of micro-galvanic couples. However, as the SKPFM results indicate the Volta potential differences are reached after approximately 10 µm into the a-phase which could explained why the corrosion is initiated in the central parts and not close to the β-phase.

We believe that oxygen reduction is the dominating cathode reaction for AZ91 under these conditions, with very thin water ad-layers on the surface. For AZ31, Strebl et al. [39] showed that oxygen reduction contributed less to the cathodic process compared to AZ91, and water reduction could be more important. For AZ31, the intermetallic AlMn particles are probably the main cathodic sites. The corrosion attack is probably less localised on AZ31 compared to AZ91, which should be linked the lower Al-content on the former. A schematic description of the initial atmospheric corrosion of AZ 91 with micro galvanic couples formed between the b-phase and the central parts of the a-phase is shown in Figure 13. However, it is also likely that AlMn intermetallics will act as cathodic sites also on AZ91 and are probably the main cathodic sites for AZ31.

 doi:10.20944/preprints202509.1467.v1

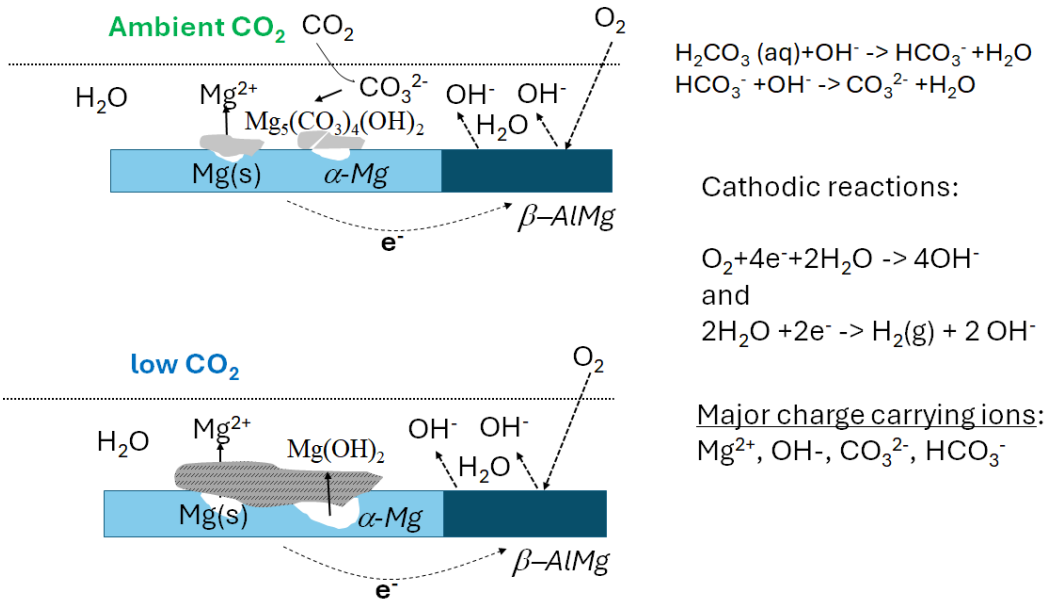

Figure 16. Schematic description of atmospheric corrosion processes on AZ91 in humid air with ambient and low CO2 content. Formation of micro-galvanic couples with β-phase and α-Mg.

5. Conclusions

The initial atmospheric corrosion of magnesium alloys AZ91 and AZ31 was investigated in pure humid air under two conditions: low CO_2 concentration (<1 ppm) and ambient CO_2 levels (≈400 ppm). The study employed in situ Infrared Reflection Absorption Spectroscopy (IRRAS), FTIR-ATR FPA imaging, Scanning Electron Microscopy with Energy Dispersive Spectroscopy (SEM-EDS), Scanning Kelvin probe force microscopy and Atomic Force Microscopy with Infrared Spectroscopy (AFM-IR).

The in situ IRRAS measurements provided insights into the composition and kinetics of corrosion product formation in humid air. Under low CO_2 conditions, $Mg(OH)_2$ was the predominant corrosion product on AZ91. In contrast, at ambient CO_2 levels, magnesium hydroxy carbonate was the dominant product, with a notably higher carbonate content observed on AZ91. For AZ31, a small amount of $Mg(OH)_2$ was also detected with ambient CO_2. Quantitative analysis of corrosion rates based on IRRAS data indicated that corrosion was significantly more severe—by an order of magnitude—in humid air with low CO_2 for both alloys. Additionally, AZ31 exhibited a higher corrosion rate than AZ91 under both low and ambient CO_2 conditions.

Initial corrosion of AZ91 was localized, primarily occurring in the central regions of the α-Mg phase, where corrosion products formation was observed, and significant Volta potential differences were measured relative to the β-phase. No significant corrosion products formation was detected on the β-phase. These findings suggest that the corrosion behavior is strongly influenced by the microstructure of AZ91, with the β-phase (AlMg) acting as the primary site for cathodic reactions and the central parts of the α-phase serving as the site for anodic processes, forming micro-galvanic cells. The lower corrosion rate observed for AZ91 is likely related to its higher aluminium content compared to AZ31.

The reduced corrosion rate in ambient CO_2 content is likely attributed to the formation of a physically blocking and more protective magnesium carbonate layer, such as hydromagnesite ($Mg_5(CO_3)_4(OH)_2{\cdot}4H_2O$). In contrast, $Mg(OH)_2$ forms a more porous and less protective layer, resulting in higher corrosion rates. Additionally, the lower solubility of magnesium carbonate may contribute to a less conductive surface electrolyte and a thinner water layer, further reducing corrosion compared to the more soluble $Mg(OH)_2$.

 doi:10.20944/preprints202509.1467.v1

Author Contributions: Conceptualization, D.P., N.L., D.T.; methodology, D.P.; software, D.P.; validation, D.P.; formal analysis, D.P.; investigation, D.P, A.W..; resources, D.P, D.T.; data curation, D.P. A.W..; writing—original draft preparation, D.P.,A.W.; writing—review and editing, D.P., DT.,N.L.; visualization, D.P., A.W.; funding acquisition, D.T., N.L., All authors have read and agreed to the published version of the manuscript.

Funding: Please This research received no external funding

Data Availability Statement: The data presented in this study are available on request from the corresponding author.

Acknowledgments: We acknowledge Oskar Karlsson, Swerim for performing SEM-EDS name.

Conflicts of Interest: The authors declare no conflicts of interestplease state "The funders had no role in the design of the study; in the collection, analyses, or interpretation of data; in the writing of the manuscript; or in the decision to publish the results".

References

1. L. Zhan, C. Kong, C. Zhao, X. Cui, L. Zhang, Y. Song, Y. Lu, L. Xia, K. Ma, H. Yang , S. Shu, B. Dong, F. Qiu, Q. Jiang, Recent advances on magnesium alloys for automotive cabin components: Materials, applications, and challenges, *J. Mater. Res. Technol.*, **2025,** 36, 9924–9961
2. M. N. Ashraf, Z. Guo, R. Wu, W. Jhiao, M. X. Chun, and A. A. Khan Gorar, Historical Progress in Electromagnetic Interference Shielding Effectiveness of Conventional Mg Alloys Leading to Mg-Li-Based Alloys: A *Review, Adv. Eng. Mater*., **2023,** 25 2300732
3. G.-L. Song, Corrosion electrochemistry of magnesium (Mg) and its alloys in: G.L. Song (Ed.), Corrosion of Magnesium Alloys, Woodhead, Cambridge, 2011, pp. 3–65.
4. E. Ghali, Activity and passivity of magnesium (Mg) and its alloys in: G.L. Song (Ed.), Corrosion of Magnesium Alloys, Woodhead, Cambridge, 2011, pp. 66–109.
5. A. Atrens, M.Liu, N.I. Zainal Abidin, G.-L. Song, Corrosion of magnesium alloys and metallurgical influence alloys in: G.L. Song (Ed.), Corrosion of Magnesium Alloys, Woodhead, Cambridge, 2011, pp. 117-1 61.
6. J.Huang, G.-L. Song, A. Atrens, M. Dargusch, What activates the Mg surface—A comparison of Mg dissolution mechanisms, *J. Mat. Sci. Technol*., **2020,** 57,204–220.
7. G.-L. Song, A. Atrens, Recently deepened insights regarding Mg corrosion and advanced engineering applications of Mg alloys, *J. Magnes. Alloys,* **2023**, 11, 3948–3991
8. M. Esmaily, J.E. Svensson, S. Fajardo, N. Birbilis, G.S. Frankel, S. Virtanen, R. Arrabal, S. Thomas, L.G. Johansson, Fundamentals and advances in magnesium alloy corrosion, *Prog. in Mater. Sci*., V89 **2017**, V89, 92-1 93.
9. H.Liu, F. Cao, G.-L. Song, D. Zheng, Z. Shi, M.S. Dargush and A. Atrens, Review of the atmospheric corrosion of magnesium alloys, *J. Mat. Sci. Technol*., **2019,** 35, 2003–2016
10. Y. Luo, L. Liu, H. Wang, T. Liu, H. Li, B. Tan, Y. Pan, A Liu, J. Cheng, Research progress on the corrosion behavior of magnesium alloys in natural environments, *Materials Today Communications* **2025**, 48, 113433
11. M. Wang, L. Yang, H. Liu, X. Wang, Y. Li, and Y. Huang, Recent Progress on Atmospheric Corrosion of Field-Exposed Magnesium Alloys, *Metals* **2024**,14, 1000.
12. R. Arrabal, A. Pardo, M. C. Merino, S. Merino, M. Mohedano and P. Casaju's, Corrosion behaviour of Mg/Al alloys in high humidity atmospheres, Mater. Corros. **2011**,62, 326-334.
13. M. Shahabi-Navid, Y. Cao, J. E. Svensson, A. Allanore, N. Birbilis, L. G. Johansson, M. Esmaily, On the early stages of localised atmospheric corrosion of magnesium–aluminium alloys, *Sci. Rep.* **2020** 10, 10:20972
14. S. Feliu Jr, A. Pardo, M.C. Merino, A.E. Coy, F. Viejo, R. Arrabal, Correlation between the surface chemistry and the atmospheric corrosion of AZ31, AZ80 and AZ91D magnesium alloys, *Appl. Surf. Sci*. **2009**, 255, 4102–4108
15. R. Lindstrom, L.-G. Johansson, G. E. Thompson, P. Skeldon, J.-E. Svensson, Corrosion of magnesium in humid air, *Corros. Sci*. 46 **2004,** 46 1141–1158

 doi:10.20944/preprints202509.1467.v1

16. M. C.Zhao, M. Liu, G. Song, A. Atrens, Influence of the β-phase morphology on the corrosion of the Mg alloy AZ91, Corrosion Science 50 (2008) 1939–1953
17. M. Jönsson and D. Persson, The influence of the microstructure on the atmospheric corrosion behaviour of magnesium alloys AZ91D and AM50, Corros. Sci. 52 (2010) 1077-1 085
18. M. Esmaily, D.B. Blücher , J.E. Svensson, M. Halvarsson, L.G. Johansson, New insights into the corrosion of magnesium alloys — The role of aluminum, Scr. Mater, 115 **2016**, 115 91–95
19. M. Danaie, R. M. Asmussen, P. Jakupi, D. W. Shoesmith, G. A. Botton, The role of aluminum distribution on the local corrosion resistance of the microstructure in a sand-cast AM50 alloy, *Corros. Sci*. **2013** 77 (151–163
20. T. M. Schwarz, N. Birbilis, B. Gault, I McCarroll, Understanding the Al diffusion pathway during atmospheric corrosion of a Mg-Al alloy using atom probe tomography, *Corros. Sci*. **2025**, 252, 112951.
21. D. Persson and C.Leygraf, I*n Situ* Infrared Reflection Absorption Spectroscopy for Studies of Atmospheric Corrosion, *J.* Electrochem. Soc. 140 **1993**, 140, 1256
22. D. Persson, D. Thierry, N. LeBozec, T. Prosek, In situ infrared reflection spectroscopy studies of the initial atmospheric corrosion of Zn–Al–Mg coated steel, *Corros. Sci*., **2013**,72, 54-63
23. D. Persson, D. Thierry, N. LeBozec, The Effect of Microstructure on Local Corrosion Product Formation during Initial SO_2-Induced Atmospheric Corrosion of ZnAlMg Coating Studied by FTIR-ATR FPA Chemical Imaging, Corros. Mater. Degrad. **2023**, 4 503-515
24. J. Mathurin, A. Deniset-Besseau, D. Bazin, E. Dartois, M. Wagner and A. Dazzi, Photothermal AFM-IR spectroscopy and imaging: Status, challenges, and trends, J. Appl. Phys. **2022**, 131, 010901.
25. V.C. Farmer, ed., The Infrared spectra of minerals, Mineralogical society, London (1974)
26. M. Jönsson, D. Persson, D.Thierry, Corrosion product formation during NaCl induced atmospheric corrosion of magnesium alloy AZ1D, Corr. Sci., **2007**, 49,1540-1 558
27. C. Fotea, J. Callaway and M.R. Alexander, Characterisation of the surface chemistry of

a. magnesium exposed to the ambient atmosphere, Surf. Interface Anal. **2006**, 38, 1363–1371

28. L. Harms, I. Brand, Application of PM IRRAS to study structural changes of the magnesium surface in corrosive environments, Vib. Spectrosc., **2018,** 97 106–113
29. A. M. Hofmeister, E. Keppel and A. K. Speck, Absorption and reflection infrared spectra of MgO and other diatomic compounds, Mon. Not. R. Astron. Soc. **2003**,345 16–38
30. B. Harbecke, B. Heinz, and P. Grosse, Optical Properties of Thin Films and the Berreman Effect, Appl. Phys. A **1985**, 38, 263-267
31. S. A. Francis and A. H. Ellison, Infrared Spectra of Monolayers on Metal Mirrors, J. Opt. Soc. Am., **1959**, 49, 131-1 38.
32. H.He, J. Cao, N. Duan, Defects and their behaviors in mineral dissolution under water environment: A review, Sci. Total Environ., **2019**, 651 2208–2217
33. Kangli Wang and Beate Paulus, Cluster Formation Effect of Water on Pristine and Defective MoS2, Monolayers, Nanomaterials **2023**, 13, 229.
34. M. Liu, S. Zanna, H. Ardelean, I. Frateur, P. Schmutz, G. Song, A. Atrens, P. Marcus, A first quantitative XPS study of the surface films formed, by exposure to water, on Mg and on the Mg–Al intermetallics: Al3Mg2 and Mg17Al12, Corros. Sci. **2009**, 51 1115–1127
35. M. Jönsson, D.Thierry, N. Lebozec, The influence of microstructure on the corrosion behaviour of AZ91D studied by scanning Kelvin probe force microscopy and scanning Kelvin probe, Corr. Sci., **2006**, 48 1193-1 208
36. M. Jönsson, D. Persson and R. Gubner, The Initial Steps of Atmospheric Corrosion on Magnesium Alloy AZ91D, *J. Electrochem. Soc*. **2007**, 154, C684
37. M. Altmaier,V. Metz, V. Neck, R. Müller, Fanghänel, Solid-liquid equilibria of $Mg(OH)_2$(cr) and $Mg_2(OH)_3Cl{\cdot}4H_2O$(cr) in the system Mg-Na-H-OH-Cl-H2O at 25°C, Geochim. Cosmochim. Acta **2003,** 67, 3595-3601
38. Q. Gautier, P. Benezeth, V. Mavromatis, J. Schott, Hydromagnesite solubility product and growth kinetics in aqueous solution from 25 to 75 ºC, Geochim. Cosmochim. Acta **2014**, 138, 1–20

 doi:10.20944/preprints202509.1467.v1

39. M. Strebl and S. Virtanen, Real-Time Monitoring of Atmospheric Magnesium Alloy Corrosion, *J. Electrochem. Soc.* 2019, 166, C3001-C3009
40. M. Strebl, M. Bruns, and S. Virtanen, Editors' Choice—Respirometric in Situ Methods for Real-Time Monitoring of Corrosion Rates: Part I. Atmospheric Corrosion, *J. Electrochem. Soc.*, **2020,** 167, 021510
41. E. Silva, S.V. Lamaka, D. Mei, M. Zheludkevich, The Reduction of Dissolved Oxygen During Magnesium Corrosion, *ChemistryOpen* **2018**, 7, 664 – 668
42. C.Wang, K. Q. Yulong Wu, D. Mei, C. Chu, F. Xue, J. Bai, M. L. Zheludkevich, S. V. Lamaka, Consistent high rate oxygen reduction reaction during corrosion of Mg-Ag Alloy, Corros. Sci., **2024**, 229, 111893